



# CHORUS

This is the accepted manuscript made available via CHORUS. The article has been published as:

## Mechanism for unconventional nonlinear elasticity

Aria Mansouri Tehrani, Amber Lim, and Jakoah Brgoch

Phys. Rev. B **100**, 060102 — Published 9 August 2019

DOI: [10.1103/PhysRevB.100.060102](https://doi.org/10.1103/PhysRevB.100.060102)

## **A mechanism for unconventional non-linear elasticity**

Aria Mansouri Tehrani and Amber Lim

*Department of Chemistry, University of Houston, Houston, TX, USA*

Jakoah Brgoch\*

*Department of Chemistry, University of Houston, Houston, TX, USA and  
Texas Center for Superconductivity, Houston, TX, USA*

Materials either have a high hardness or excellent ductility, but rarely both at the same time.  $\text{Mo}_2\text{BC}$  is one of the only crystalline materials that simultaneously has a high Vickers hardness and is also moderately ductile. The origin of this unique balance is revealed here using stress-strain calculations. The results show an anisotropic non-linear elastic response including an intermediate tensile strain-stiffening behavior and a two-step sequential failure under shear strain that resembles the behavior of soft materials like biological systems or polymer networks rather than hard, refractory metals. The mechanism of the unusual non-linear elasticity is established by analyzing changes in the electronic structure and the chemical bonding environments under mechanical perturbation. The optimized structure under extreme strain shows the formation of a pseudogap in DOS and dimerization of the structure's boron-boron zigzag chain. These mechanisms delay the ultimate failure establishing a new pathway for developing the next generation of structural materials with high hardness and ductility.

## I. INTRODUCTION

The balance of hardness and ductility is an essential materials consideration for every application.<sup>1-4</sup> Cutting tools and wear resistant coatings require high hardness while brittleness can adversely affect their working lifespan due to the formation and propagation of cracks.<sup>5,6</sup> Yet, developing new compounds with both high hardness and excellent ductility is extremely challenging because nearly all materials are typically either hard and brittle or ductile and soft.<sup>3,4,7</sup> Researchers have devised some approaches to overcome this trade-off, especially for crystalline inorganic solids. For example, the formation of ordered oxygen complexes can simultaneously enhance the strength and ductility in a class of high entropy alloys through a strain-hardening mechanism.<sup>8</sup> Another research route to acquire high hardness and ductility is through the development of damage-tolerant architected materials. The various periodic arrangement of these materials can yield many unconventional mechanical properties, such as negative Poisson's ratio as well as materials with fine-tuned high strength and toughness.<sup>9</sup> Varying the grain structure through extensive processing is also an avenue towards high hardness systems with moderate ductility by enhancing hardening mechanisms that work on longer length scales such as dislocation pinning.<sup>10</sup> Further, an increase in ductility has also been reported by engineering the stacking fault energies to limit the possible deformation modes in transition metals monocarbides.<sup>11</sup>

There are significantly fewer examples of influencing the hardness/ductility based solely on modifying the structure or chemical bonding in simple crystalline solids. DFT calculations have shown that alloying the TiN with Mo and W enhances the toughness significantly.<sup>12</sup> The system Mo<sub>2</sub>BC also provides an opportunity to investigate a pseudo-layered crystal structure with an extremely high hardness (29 GPa *via* nanoindentation<sup>13</sup>) that is moderately ductile. Indeed, given the chemical composition, this phase has a much higher than expected ductility based on its Pugh's ratio falling on the border of the ductile regime ( $G/B = \approx 0.57$ ), the positive Cauchy pressure,<sup>13</sup> and by in situ analysis of crack behavior during tensile testing.<sup>14</sup> As a result, Mo<sub>2</sub>BC is considered for application as a hard coating due to its high hardness, high fracture toughness, and relative ductility.<sup>6,13</sup> However, identifying the fundamental origins of plasticity in this phase or other metal-rich materials with complex crystal structures remains elusive due to challenges in controlling sample preparation and testing conditions. Some progress has been made by developing small-scale testing methods such as micro-compression to study plasticity in hard materials.<sup>15</sup> Additionally, first-principles calculations have provided insight into the structure-mechanical property relationships in materials, such as ternary carbides and borides.<sup>16-18</sup> Nevertheless, research applying these experimental or computational techniques to develop entirely new materials systems is limited owing to the difficulties associated with the experimental measurements and computational cost of simulating complex mechanical processes like indentation.<sup>19</sup> More recently, a machine learning based screening method provides an approach to identify potential high hardness materials *a priori*.<sup>20</sup> For example, predicting the bulk ( $B$ ) and shear ( $G$ ) moduli (of 118,287 compounds) as a proxy for hardness recommended the further examination of a transition metal carbide, ReWC<sub>0.8</sub>, and Mo<sub>0.9</sub>W<sub>1.1</sub>BC.<sup>20</sup> Even though  $B$  and  $G$  are correlated with both hardness and ductility, the elastic moduli only pertain to small strains at equilibrium. On the contrary, the severe deformation of these materials lead to large strains and non-equilibrium conditions, which cannot be adequately explained by elastic moduli.<sup>21,22</sup> Thus, to fully understand the mechanisms governing deformation in a new material identified using high-level techniques like machine learning, a more comprehensive analysis is necessary.

One solution is to employ *ab-initio* calculations of stress-strain behavior as a probe of materials at large strains. These calculations can be used to determine the yield strength as an upper bound for the strength of a defect-free crystal.<sup>21,23</sup> In fact, this idea has been used to explain the deformation response of Al and Cu metals,<sup>22</sup> determine the elastic instability in transition metal carbides and nitrides (HfC, TiN, and TiC),<sup>17</sup> study differences in the atomistic deformation modes of diamond, *c*-BN, and BC<sub>2</sub>N,<sup>24</sup> and understand how carbon content affects the strength of BC<sub>*x*</sub>N.<sup>25</sup> Moreover, these calculations identified an unexpected strain-stiffening mechanism in Fe<sub>3</sub>C and Al<sub>3</sub>BC<sub>3</sub>, which resembles the mechanical behavior of biological materials, such as skin.<sup>26</sup> More recently, two tungsten nitrides, hp4-WN and hp6-WN<sub>2</sub> were also predicted using crystal structure searching algorithms and suggested to have a hardness of >40 GPa, even in the asymptotic regime based on their high calculated ultimate stress. The extremely high hardness of these predicted nitrides is attributed to indentation compression induced strengthening and the strengthening of tungsten-tungsten bonds.<sup>27</sup> Finally, stress-strain calculations revealed that a sequential bond-breaking mode was responsible for outstanding mechanical properties of the hypothetical *d*-BC<sub>3</sub>.<sup>28</sup>

In our work to understand the mechanical properties and structural chemistry of transition metal borocarbides previously selected using machine learning, we explore the mechanical behavior of the compound and identify a previously unobserved intermediate strain-stiffening mechanism in a material with high hardness. Mo<sub>2</sub>BC experiences an electronic structure-mediated two-step failure during deformation. This response is different compared to all other typical brittle, hard materials such as ReB<sub>2</sub> and diamond. The results more closely resemble biological systems like collagen, soft materials such as cross-linked rubber and polymer networks,<sup>29-31</sup> or annealed AISI 1040 steel.<sup>31</sup> The mechanism of the observed intermediate strain-stiffening under tension stems from the formation of electronic pseudo-gap in the density of state under strain whereas a delayed failure during shear deformation occurs based

on an initial dimerization of the B-B zigzag chains followed by the strengthening of these dimers. The evolution of this compound's electronic structure and its chemical bonding environments during the deformation produce the non-linear elongation of the stress-strain curve. The findings of this research not only explain the fundamental mechanisms governing the mechanical response in Mo<sub>2</sub>BC, but it also provides a new perspective on the design of future structural materials by contradicting the notion of avoiding anisotropic materials with pseudo-layered crystal structures.

To study the fundamental structural-mechanical properties of Mo<sub>2</sub>BC, the DFT stress-strain behavior was evaluated for numerous crystalline directions and planes. For the computational methods see the Supplemental Material.<sup>32-42</sup> The optimized crystal structure of Mo<sub>2</sub>BC (space group *Cmcm*) is illustrated in Fig. 1a and contains infinite zig-zag chains of boron atoms along the [001] direction that alternate with layers of molybdenum atoms that center the basal plane of a square-based pyramid. For stress-strain analysis, as the crystal is strained the stress is typically increases until reaching a maximum value, which is designated as the ideal (ultimate) tensile/shear stress (strength). The computational results for Mo<sub>2</sub>BC, plotted in Fig. 1b, depict the uniaxial tensile stress-strain curves for the high symmetry directions. Similar to the anisotropy observed in this orthorhombic crystal structure, the mechanical response is also highly anisotropic. The lowest stress tolerated by the structure occurs for the [010] and [011] directions, which achieves a maximum of only  $\approx 30$  GPa at 0.15 strain. These directions show the commonly observed linear increase in stress before reaching a plateau followed by a sudden drop at failure. The ultimate stress occurs for the [100] direction reaching  $\approx 60$  GPa at 0.46 strain followed closely by [001] with a value of  $\approx 56$  GPa at 0.49 strain. These two directions are exceptionally separated from the other directions and show a comparatively much higher ultimate stress and strain. In fact, the ultimate strength of these two directions in Mo<sub>2</sub>BC is only slightly lower than superhard materials like ReB<sub>2</sub>, which range from  $\approx 48$  GPa for ( $\bar{1}3\bar{1}0$ ) to  $\approx 76$  GPa for (0001).<sup>43</sup> A closer analysis of the [001] and [100] tension directions also highlights an entirely different mechanical behavior exhibiting an intermediate strain-induced stiffening that is more commonly observed in polymers, biological materials, and hydrogels. As these material are strained, they get stiffer.<sup>44,45</sup> The strain-induced stiffening in the crystalline material studied here is somewhat similar to cementite (Fe<sub>3</sub>C) during shear deformation, which is the origin of its robust mechanical behavior; yet, cementite is significantly softer with Vickers hardness of only  $\approx 10$  GPa compared with 29 GPa measured *via* nanoindentation for Mo<sub>2</sub>BC.<sup>26</sup>

Similarly, the mechanical behavior of Mo<sub>2</sub>BC is also investigated under shear stress because indentation occurs through plastic deformation, which is governed by the movement of dislocations that only glide under shear strain.<sup>46</sup> For highly anisotropic materials such as MAX phases,<sup>47</sup> the hardest slip plane is known to dictate indentation resistance whereas the softest slip system is responsible for the failure of the material. Identifying the softest or hardest slip planes require an exhaustive probe of the different slip systems. These calculations are provided in Table S1 of the Supplemental Material.<sup>32</sup> The highest ideal shear stress in Mo<sub>2</sub>BC is achieved for the (110)[ $\bar{1}10$ ] shear slip system with an ideal stress of 50 GPa while the highest strain of 0.37 occurring for the (110)[ $\bar{1}\bar{1}1$ ] slip system. These properties are competitive with other high hardness materials such as ReB<sub>2</sub>, where the highest ideal shear stress is 52 GPa at 0.27 strain.<sup>16</sup> Even though the ideal shear in ReB<sub>2</sub> is slightly higher than Mo<sub>2</sub>BC, the corresponding shear strain in Mo<sub>2</sub>BC is significantly higher, further emphasizing its ductility. It should be noted that while high strains indicate a ductile behavior, ductility is a complicated property that is influenced by many other factors such as a competition between crack propagation and dislocation nucleation.<sup>48</sup> However, these analysis are outside of the scope of the current manuscript.

Additional calculations indicate the softest shear plane in Mo<sub>2</sub>BC is (111)[ $\bar{1}\bar{1}2$ ] with ideal stress of 20 GPa at 0.28 strain. For comparison, the softest slip system in OsB<sub>2</sub> during shear deformation is only  $\approx 9$  GPa,<sup>49</sup> half of this borocarbide. However, the softest shear in ReB<sub>2</sub> is 36 GPa at 0.18 strain, indicating the hardness of Mo<sub>2</sub>BC falls between these two diborides, in agreement with experimental observations. This shear stress-strain curve also shows a striking two-step progression before eventual failure. As illustrated in Fig. 1c, the stress increases as a function of strain before beginning to decrease at approximately 0.19 strain. At this point, the material would be expected to fail; however, an atypical increase in the stress then occurs extending the strain until eventual ultimate failure at 0.3 strain with a stress of 20 GPa. This delayed failure during shear deformation provides a  $\approx 35\%$  improvement in the fracture strain tolerated by the structure, which contributes to the ductile nature of Mo<sub>2</sub>BC.

The origin of this unique strain-stiffening behavior was resolved by examining the electronic structure of Mo<sub>2</sub>BC under mechanical perturbation. First, the [001] tensile direction, which could be a key component of the mechanical properties in Mo<sub>2</sub>BC, was investigated. Plotting the [001] stress-strain curve in Fig. 2 shows it can be divided into three distinct stages (up to 0.53 strain). The curve's first stage occurs between strains 0-0.1, the second stage is between strains 0.1-0.25, and the third stage falls from strains 0.25-0.5. The corresponding density of states (DOS) at multiple strain steps for each stage have also been plotted and color-coded in Fig. 2 to illustrate the electronic structure perturbations as the structure is strained. Fig. 2a shows that in the first stage, the stress increases almost linearly as the compound is strained, which follows conventional stress-strain behavior of crystalline metals and ceramics with a parabolic work-hardening.<sup>31</sup> The corresponding DOS curve shows the metallic behavior of Mo<sub>2</sub>BC with the Fermi level ( $E_f$ ) residing on a shoulder, dominated by  $4d$  orbitals of Mo as shown by Fig. S3 in Supplemental Material.<sup>32</sup>

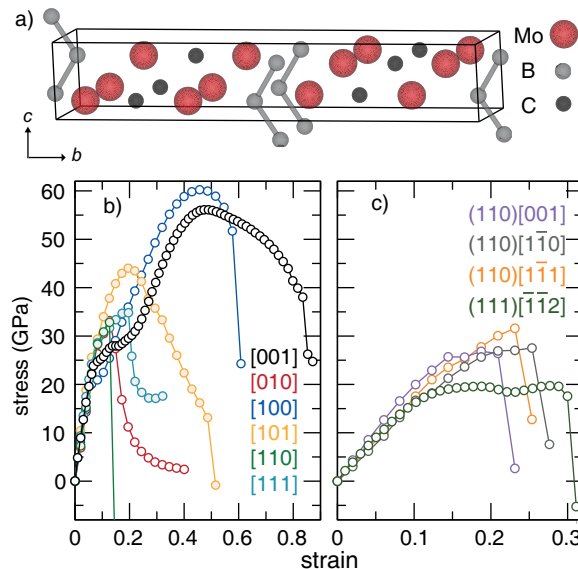


FIG. 1. a) Crystal structure of  $\text{Mo}_2\text{BC}$ . b) Calculated stress-strain curves for various crystallographic directions during applied tension. c) Stress-strain curve for various shear systems.

As the compound is strained, the DOS undergoes minor changes with  $E_f$  shifting to lower energy owing to differences in the bond lengths followed by unit cell volume expansion. As the compound is further strained in the final steps of the first stage, a small local maximum appears in the DOS at  $E_f$  (strain 0.14 in Fig. 2b) indicating a potential electronic instability. At this point, a dramatic decrease in the stress-strain curve would be expected, and the material should fail as shown by a drop in the stress. However, instead of failure the curve merely flattens as the compound enters the second strain stage (Fig. 2c). This process coincides with the formation of a pseudogap at  $E_f$  for 0.16 strain, shown in Fig. 2d. The structure overcomes the energetic barrier imposed from the strain through the intrinsic formation of an electronically stabilizing pseudogap. This prevents the anticipated failure of  $\text{Mo}_2\text{BC}$  at this point and allows the structure to accommodate additional strain. The pseudogap in the DOS remains through the end of the second stage of the stress-strain curve. Proceeding to the third stage, illustrated in Fig. 2e, shows the stress starts to increase again until reaching the ideal stress and strain at 56 GPa and 0.47, respectively, (Fig. 2c). Correspondingly,  $E_f$  moves to the shoulder of the pseudogap in DOS (Fig. 2f) prior to falling on a peak at strain 0.50 at which point the compound is mechanically and electronically unstable with no possibility for a second recovery. The formation of a pseudogap in the DOS during the second stage provides mechanistic support for the observed intermediate strain-stiffening. Nevertheless, this phenomenon is just one component of the simultaneous high hardness and ductility in  $\text{Mo}_2\text{BC}$ .

Further unraveling the mechanism of failure in  $\text{Mo}_2\text{BC}$  requires also understanding the two-step behavior of the  $(111)[\bar{1}\bar{1}2]$  shear stress-strain curve. Analyzing the DOS curves for the  $(111)[\bar{1}\bar{1}2]$  shear system does not indicate the similar opening of a pseudogap (Fig. S2 in Supplemental Material<sup>32</sup>) suggesting this unique stress-strain curve stems from a different mechanism. The most likely culprit in this case are changes in the crystal structure and chemical bonding during the deformation. Fig. 3a depicts superimposed snapshots of the  $\text{Mo}_2\text{BC}$  crystal structure under  $(111)[\bar{1}\bar{1}2]$  shear deformation with increasing strain. As shown by the strain steps highlighted in Fig. 3b, the evolution of the unit cell and atomic coordinates along the deformation path indicate the most notable changes occur for the boron bonding network. Specifically, under shear strain, the structure's symmetry breaks allowing the B-B interactions to split into two nonequivalent B1-B2 and B1-B3 interactions. Initially, at zero strain, the boron-boron bond lengths are all equal and separated by 1.83 Å. As the crystal structure is strained the B1-B2 interatomic distance increases from 1.87 Å at 0.05 strain to 2.49 Å at 0.26 strain. This distance is sufficient to consider the bond effectively broken. However, at the same time, the B1-B3 interaction actually undergoes a decrease in bond length shortening from 1.85 Å at 0.05 strain to 1.83 Å at 0.26 strain. This asymmetric progression of the bond lengths is representative of dimerization of the boron-boron interactions, which is visualized in Fig. 3a with the increase in B1-B2 interatomic distance indicated by the absence of a bond at strains  $>0.13$  whereas the B1-B3 bond remains for all strain steps.

A quantitative analysis of changes among the interatomic interactions can be made by decomposing the DOS into the bonding and antibonding components based on a crystal orbital Hamilton population ( $-\text{COHP}$ ) analysis (Fig. S2 in Supplemental Material<sup>32</sup>).<sup>41,42</sup> Evaluating the evolution of the interatomic interactions along the  $(111)[\bar{1}\bar{1}2]$  shear deformation path, the integrated  $-\text{COHP}$  ( $-\text{ICOHP}$ ) values, which tend to scale with the strength of the interactions,

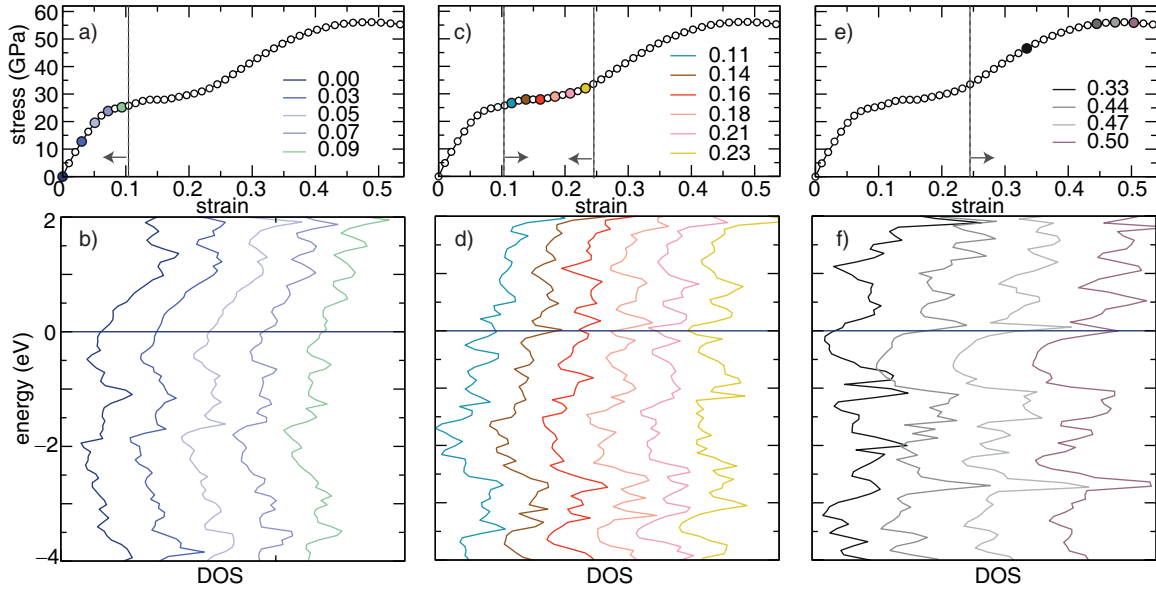


FIG. 2. The stress-strain curve for [001] in  $\text{Mo}_2\text{BC}$  is segmented into three interdependent stages. a) Stage 1 of the stress-strain curve is plotted with the highlighted strain steps corresponding b) the density of state (DOS) of Stage 1. c) Shows the Stage 2 with the color-coded points corresponding to d) the DOS of Stage 2. e) Stage 3 shows the final stage of the stress-strain curve and the colors correspond to f) different strain steps in the DOS of Stage 3.

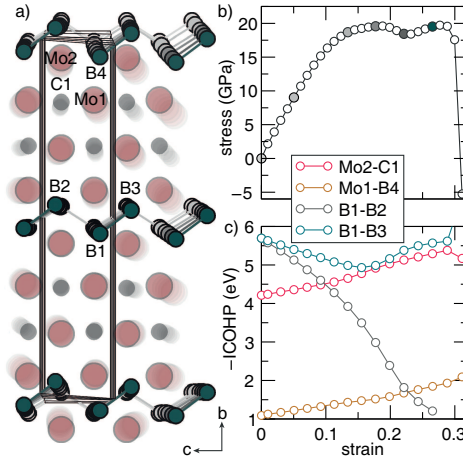


FIG. 3. a) Stacked snapshots of the crystal structure of  $\text{Mo}_2\text{BC}$  during  $(111)[\bar{1}\bar{1}2]$  deformation at shear strain steps of 0, 0.05, 0.13, 0.18, 0.22, and 0.26. b) Stress-strain behavior of  $\text{Mo}_2\text{BC}$  under  $(111)[\bar{1}\bar{1}2]$  shear deformation and c)  $-\text{ICOHP}$  values as a function of strain during  $(111)[\bar{1}\bar{1}2]$  shear for various interactions.

were calculated and are plotted as a function of strain in Fig. 3c. From these data it is clear the loss of symmetry allows the B-B interactions to independently change leading to substantial changes in the chemical bonding with the most notable being a  $\approx 79\%$  decrease of the  $-\text{ICOHP}$  values for the B1-B2 interaction at maximum strain (Fig. 3c). Exploring the fluctuations in the other  $-\text{ICOHP}$  values during the shear deformation makes it clear the B1-B2 contact weakens the most. Perturbing the structure further, causes the B1-B2 contact to continue a nearly linear decrease to only  $\approx 1$  eV/bond. Such a dramatic loss of covalent bonding character usually is sufficient to cause a structure to fail. However, analyzing the B1-B3  $-\text{ICOHP}$  value shows this drops by only 0.76 eV/bond, which is only half of the 2.19 eV/bond decrease calculated for the B1-B2 interaction up to a strain of 0.18. Moreover, the  $-\text{ICOHP}$  value for the B1-B3 contact under additional strain unexpectedly begins to increase with greater strain reaching a maximum of 5.5 eV/bond at strain 0.26. This is nearly equivalent to the unstrained crystal structure (5.69 eV/bond). The transition of the B1-B3  $-\text{ICOHP}$  value from decreasing, indicating a weakening of the interaction, to increasing, indicating a strengthening of the interaction, is directly correlated with the structure's mechanical properties.

It is clear that the first drop in the stress-strain curve occurs as the boron zigzag chain begins to dimerize. The B1-B3 dimer, however, begins to strengthen as implied by a shortening of the bond length as well as an increase in  $-ICOHP$  value. Moreover, Fig. 3c also highlights an increase in the  $-ICOHP$  values for the Mo2-C1 and Mo1-B4 contacts by  $\approx 25\%$  and  $\approx 70\%$ , respectively, as the structure is strained. It is also worth noting that the  $-ICOHP$  values are more significant for the Mo-C interactions compared to the Mo-B interactions, in agreement to the more substantial hybridization of Mo-C  $4d-2p$  orbitals versus Mo-B  $4d-2p$  orbital, as determined from the partial DOS (Fig S1 in Supplemental Material<sup>32</sup>). This culmination of changes in the electronic structure leads to the formation of an electronically metastable state for Mo<sub>2</sub>BC with chemical bonds that are actually enhanced by straining the crystal structure.

In summary, the non-linear elastic stress-strain behavior in Mo<sub>2</sub>BC supports the compound's high hardness while also bearing surprising ductility. This unanticipated mechanical response stems from an observed strain stiffening, which is explained through the formation of an electronic pseudogap within the DOS and dimerization of the boron-boron zigzag interactions. The tensile strain-stiffening along [001] enhances its ultimate strength and strain while the sequential bond breakage along (111)[ $\bar{1}\bar{1}2$ ] contribute to the unexpected ductility. The insight gained from this study not only provides a mechanistic answer for the unique non-linear elasticity observed in Mo<sub>2</sub>BC, but it also provides a better understanding of the complex and relatively unexplored intrinsic mechanical behavior of transition-metal borocarbides and more specifically crystalline solids with intriguing and uncommon mechanical properties.

## II. ACKNOWLEDGMENTS

The authors gratefully acknowledge the generous financial support provided by the National Science Foundation through No. NSF-CMMI 15-62142 and the donors of the American Chemical Society Petroleum Research Fund (55625-DNI10) for supporting this research. Support for this work was provided by resources of the uHPC cluster managed by the University of Houston and acquired through NSF Award Number 15-31814. This research also used the Maxwell and Opuntia Clusters operated by the University of Houston and the Center for Advanced Computing and Data Systems.

---

\* jbrgoch@uh.edu

- <sup>1</sup> R. O. Ritchie, "The conflicts between strength and toughness," *Nat. Mater.* **10**, 817–822 (2011).
- <sup>2</sup> Y. Wei, Y. Li, L. Zhu, Y. Liu, X. Lei, G. Wang, Y. Wu, Z. Mi, J. Liu, H. Wang, and H. Gao, "Evading the strength-ductility trade-off dilemma in steel through gradient hierarchical nanotwins," *Nat. Commun.* **5**, 3580 (2014).
- <sup>3</sup> S. H. Kim, H. Kim, and N. J. Kim, "Brittle intermetallic compound makes ultrastrong low-density steel with large ductility," *Nature* **518**, 77–79 (2015).
- <sup>4</sup> J. Ye, Y. M. Wang, R. T. Ott, Z. Zeng, J. T. McKeown, P. J. Depond, M. K. Santala, T. T. Roehling, T. Zhu, N. P. Calta, M. J. Matthews, Y. Zhang, Z. Li, W. Chen, A. V. Hamza, and T. Voisin, "Additively manufactured hierarchical stainless steels with high strength and ductility," *Nat. Mater.* **17**, 63–71 (2017).
- <sup>5</sup> K. Nakayama, M. Arai, and T. Kanda, "Machining characteristics of hard materials," *CIRP Ann. - Manuf. Technol.* **37**, 89–92 (1988).
- <sup>6</sup> R. Soler, S. Gleich, C. Kirchlechner, C. Scheu, J. M. Schneider, and G. Dehm, "Fracture toughness of Mo<sub>2</sub>BC thin films: Intrinsic toughness versus system toughening," *Mater. Des.* **154**, 20–27 (2018).
- <sup>7</sup> Y. X. Wang and S. Zhang, "Toward hard yet tough ceramic coatings," *Surf. Coatings Technol.* **258**, 1–16 (2014).
- <sup>8</sup> J. Liu, S. Jiang, Z. Lu, X. Hui, K. An, H. Chen, Q. Zeng, D. Raabe, T.-G. Nieh, H. Wang, Y. Wu, Y. Wu, S. Wang, Q. Zhang, P. Kontis, L. Gu, B. Gault, Z. Lei, H. Wang, and X. Liu, "Enhanced strength and ductility in a high-entropy alloy via ordered oxygen complexes," *Nature* **563**, 546–550 (2018).
- <sup>9</sup> M. S. Pham, C. Liu, I. Todd, and J. Lertthanasarn, "Damage-tolerant architected materials inspired by crystal microstructure," *Nature* **565**, 305–311 (2019).
- <sup>10</sup> F. Yuan, X. Wu, M. Yang, G. Wu, X. Huang, Y. Wei, and Y. Zhu, "Heterogeneous lamella structure unites ultrafine-grain strength with coarse-grain ductility," *Proc. Natl. Acad. Sci.* **112**, 14501–14505 (2015).
- <sup>11</sup> N. De Leon, X. X. Yu, H. Yu, C. R. Weinberger, and G. B. Thompson, "Bonding effects on the slip differences in the B1 monocarbides," *Phys. Rev. Lett.* **114**, 165502 (2015).
- <sup>12</sup> D. G. Sangiovanni, V. Chirita, and L. Hultman, "Electronic mechanism for toughness enhancement in Ti<sub>x</sub>M<sub>1-x</sub>N (M = Mo and W)," *Phys. Rev. B* **81**, 104107 (2010).
- <sup>13</sup> J. Emmerlich, D. Music, M. Braun, P. Fayek, F. Munnik, and J. M. Schneider, "A proposal for an unusually stiff and moderately ductile hard coating material: Mo<sub>2</sub>BC," *J. Phys. D: Appl. Phys.* **42**, 185406 (2009).
- <sup>14</sup> S. Djaziri, S. Gleich, H. Bolvardi, C. Kirchlechner, M. Hans, C. Scheu, J. M. Schneider, and G. Dehm, "Are Mo<sub>2</sub>BC nanocrystalline coatings damage resistant? Insights from comparative tension experiments," *Surf. Coatings Technol.* **289**, 213–218 (2016).

- 15 S. Korte-Kerzel, "Microcompression of brittle and anisotropic crystals: Recent advances and current challenges in studying plasticity in hard materials," *MRS Commun.* **7**, 109–120 (2017).
- 16 C. Zang, H. Sun, J. S. Tse, and C. Chen, "Indentation strength of ultraincompressible rhenium boride, carbide, and nitride from first-principles calculations," *Phys. Rev. B - Condens. Matter Mater. Phys.* **86**, 14108 (2012).
- 17 S. H. Jhi, S. G. Louie, M. L. Cohen, and J. W. Morris, "Mechanical instability and ideal shear strength of transition metal carbides and nitrides," *Phys. Rev. Lett.* **87**, 75503–1–75503–4 (2001).
- 18 J. Yang, H. Sun, and C. Chen, "Anomalous strength anisotropy of  $\gamma$ -Fe<sub>4</sub>N identified by first-principles calculations," *Appl. Phys. Lett.* **94**, 151914 (2009).
- 19 A. Mansouri Tehrani and J. Brgoch, "Hard and superhard materials: A computational perspective," *J. Solid State Chem.* **271**, 47–58 (2019).
- 20 A. Mansouri Tehrani, A. O. Oliylyk, M. Parry, Z. Rizvi, S. Couper, F. Lin, L. Miyagi, T. D. Sparks, and J. Brgoch, "Machine Learning Directed Search for Ultraincompressible, Superhard Materials," *J. Am. Chem. Soc.* **140**, 9844–9853 (2018).
- 21 J. W. Morris, M. L. Cohen, D. Roundy, D. C. Chrzan, and C. R. Krenn, "Connecting atomistic and experimental estimates of ideal strength," *Phys. Rev. B* **65**, 1–4 (2002).
- 22 S. Ogata, J. Li, and S. Yip, "Ideal pure shear strength of aluminum and copper," *Science* **298**, 807–811 (2002).
- 23 D. Roundy, C. R. Krenn, M. L. Cohen, and J. W. Morris, "Ideal shear strengths of fcc aluminum and copper," *Phys. Rev. Lett.* **82**, 2713–2716 (1999).
- 24 Y. Zhang, H. Sun, and C. Chen, "Atomistic deformation modes in strong covalent solids," *Phys. Rev. Lett.* **94** (2005), 10.1103/PhysRevLett.94.145505.
- 25 Y. Zhang, H. Sun, and C. Chen, "Influence of carbon content on the strength of cubic BC<sub>x</sub>N: A first-principle study," *Phys. Rev. B* **77**, 094120 (2008).
- 26 C. Jiang and S. G. Srinivasan, "Unexpected strain-stiffening in crystalline solids," *Nature* **496**, 339–342 (2013).
- 27 C. Lu, Q. Li, Y. Ma, and C. Chen, "Extraordinary indentation strain stiffening produces superhard tungsten nitrides," *Phys. Rev. Lett.* **119**, 115503 (2017).
- 28 M. Zhang, H. Liu, Q. Li, B. Gao, Y. Wang, H. Li, C. Chen, and Y. Ma, "Superhard BC<sub>3</sub> in Cubic Diamond Structure," *Phys. Rev. Lett.* **114**, 015502 (2015).
- 29 R. F. Zhang, D. Legut, R. Niewa, A. S. Argon, and S. Veprek, "Shear-induced structural transformation and plasticity in ultraincompressible ReB<sub>2</sub> limit its hardness," *Phys. Rev. B* **82** (2010).
- 30 Y. Zhang, Sun Hong, and C. Chen, "Superhard cubic BC<sub>2</sub>N compared to diamond," *Phys. Rev. Lett.* **93** (2004), 10.1103/PhysRevLett.93.195504.
- 31 M. A. Meyers and K. K. Chawla, *Mechanical behavior of materials* (Cambridge University Press, 2009) p. 856.
- 32 "See Supplemental Material at [URL] which includes Refs. [33-42] for the description of the computational methods used here as well as DOS and COHP figures of Mo<sub>2</sub>BC and a table of ideal stress and strain values for various shear systems."
- 33 G. Kresse and J. Furthmüller, "Efficient iterative schemes for ab initio total-energy calculations using a plane-wave basis set," *Phys. Rev. B* **54**, 11169–11186 (1996).
- 34 D. Joubert, "From ultrasoft pseudopotentials to the projector augmented-wave method," *Phys. Rev. B - Condens. Matter Mater. Phys.* **59**, 1758–1775 (1999).
- 35 P. E. Blöchl, "Projector augmented-wave method," *Phys. Rev. B* **50**, 17953–17979 (1994).
- 36 J. P. Perdew, K. Burke, and M. Ernzerhof, "Generalized gradient approximation made simple," *Phys. Rev. Lett.* **77**, 3865–3868 (1996).
- 37 H. J. Monkhorst and J. D. Pack, "Special points for Brillouin-zone integrations," *Phys. Rev. B* **13**, 5188–5192 (1976).
- 38 G. S. Smith, A. G. Tharp, and Q. Johnson, "Determination of the light-atom positions in Mo<sub>2</sub>BC," *Acta Crystallogr. Sect. B Struct. Crystallogr. Cryst. Chem.* **25**, 698–701 (2002).
- 39 J. Hao, J. S. Tse, S. Lu, H. Liu, and Y. Li, "High-energy density and superhard nitrogen-rich B-N compounds," *Phys. Rev. Lett.* **115**, 105502 (2015).
- 40 M. Zhang, M. Lu, Y. Du, L. Gao, C. Lu, and H. Liu, "Hardness of FeB<sub>4</sub>: Density functional theory investigation," *J. Chem. Phys.* **140**, 174505 (2014).
- 41 R. Dronskowski and P. E. Blöchl, "Crystal orbital hamilton populations (COHP). Energy-resolved visualization of chemical bonding in solids based on density-functional calculations," *J. Phys. Chem.* **97**, 8617–8624 (1993).
- 42 S. Maintz, V. L. Deringer, A. L. Tchougréeff, and R. Dronskowski, "LOBSTER: A tool to extract chemical bonding from plane-wave based DFT," *J. Comput. Chem.* **37**, 1030–1035 (2016).
- 43 J. Wang and Y. J. Wang, "Mechanical and electronic properties of 5d transition metal diborides M B<sub>2</sub> (M=Re, W, Os, Ru)," *J. Appl. Phys.* **105**, 083539 (2009).
- 44 K. A. Erk, K. J. Henderson, and K. R. Shull, "Strain stiffening in synthetic and biopolymer networks," *Biomacromolecules* **11**, 1358–1363 (2010).
- 45 M. Jaspers, M. Dennison, M. F. Mabesoone, F. C. MacKintosh, A. E. Rowan, and P. H. Kouwer, "Ultra-responsive soft matter from strain-stiffening hydrogels," *Nat. Commun.* **5**, 5808 (2014).
- 46 J. Gilman, *Electronic basis of the strength of materials* (Cambridge University Press, 2003) p. 280.
- 47 M. W. Barsoum and M. Radovic, "Elastic and mechanical properties of the max phases," *Annual review of materials research* **41**, 195–227 (2011).
- 48 S. Zhou, D. Beazley, P. Lomdahl, and B. Holian, "Large-scale molecular dynamics simulations of three-dimensional ductile failure," *Physical Review Letters* **78**, 479 (1997).
- 49 J. Yang, H. Sun, and C. Chen, "Is osmium diboride an ultra-hard material?" *J. Am. Chem. Soc.* **130**, 7200–7201 (2008).